Journal of Computational Physics **152,** 584–607 (1999)
Article ID jcph.1999.6246, available online at http://www.idealibrary.com on IDEAL®

An SPH Projection Method

Sharen J. Cummins* and Murray Rudman†

*Department of Mathematics and Statistics, Monash University, Clayton, Victoria 3168, Australia; and †CSIRO Building Construction and Engineering, Highett, Victoria 3122, Australia
E-mail: *sharen@groucho.maths.monash.edu.au and †Murray.Rudman@dbce.csiro.au

Received September 16, 1998; revised February 19, 1999

A new formulation is introduced for enforcing incompressibility in Smoothed Particle Hydrodynamics (SPH). The method uses a fractional step with the velocity field integrated forward in time without enforcing incompressibility. The resulting intermediate velocity field is then projected onto a divergence-free space by solving a pressure Poisson equation derived from an approximate pressure projection. Unlike earlier approaches used to simulate incompressible flows with SPH, the pressure is not a thermodynamic variable and the Courant condition is based only on fluid velocities and not on the speed of sound. Although larger time-steps can be used, the solution of the resulting elliptic pressure Poisson equation increases the total work per time-step. Efficiency comparisons show that the projection method has a significant potential to reduce the overall computational expense compared to weakly compressible SPH, particularly as the Reynolds number, *Re*, is increased. Simulations using this SPH projection technique show good agreement with finite-difference solutions for a vortex spin-down and Rayleigh–Taylor instability. The results, however, indicate that the use of an approximate projection to enforce incompressibility leads to error accumulation in the density field.

1. INTRODUCTION

Smoothed particle hydrodynamics (SPH) is a fully Lagrangian, particle-based technique that has typically been used to simulate the motion of compressible fluids. It was originally developed for astrophysical applications [12, 20] but has since been extended to model a wide range of problems including multi-phase flows [23], deformation and impact problems [34], and heat conduction [8]. More recently it has been extended and used to simulate the motion of incompressible fluids [24, 27]. Incompressibility is approximated in [24, 27] by assuming a compressible fluid with a large sound speed—typically a Mach number of $M \approx 0.1$ is used. This approach will be termed here "weakly compressible" SPH or "WCSPH" and results obtained using this approach have been acceptable for free surface and some low Reynolds number flows, although not for fully confined moderate and high

0021-9991/99 $30.00

Reynolds number flows. Compressibility causes problems with sound wave reflection at the boundaries and the high sound speed leads to a crippling CFL time-step constraint.

A different approach to modeling free surface, incompressible flows using a fully Lagrangian technique was the particle method proposed by Koshizuka *et al.* [17], where a penalty-like formulation was employed to adjust the pressure where density variations occurred. An iterative process that converged when density changes were below a specified tolerance was used. A similar approach was used in [18], where a pressure Poisson equation was solved instead of a penalty method with source term proportional to density variations. It is not clear though how efficient or accurate these methods are for free surface modeling compared to the use of WCSPH.

More traditional approaches to solving the incompressible Navier–Stokes equations on Eulerian grids often use an explicit projection to enforce incompressibility. Originally developed in [7] and later adapted in [4], the projection approach has been employed extensively in grid-based methods such as finite-difference [1, 5] and finite elements [14], but it has not been extended to the SPH environment.

In this paper, a technique that enforces incompressibility in SPH by employing an approximate pressure projection is described. The method utilizes a fractional step with the velocity field first integrated forward in time without enforcing incompressibility. The resulting intermediate velocity field is projected onto a divergence-free space by solving a pressure Poisson equation. Because the method uses an incompressible formulation, sound waves are not admitted and the CFL condition is based purely on the fluid velocity field, allowing use of time steps significantly larger than those used in WCSPH. Although the allowable time-step increases when a pressure projection is employed, the projection step requires solution of an elliptic problem, and the amount of work per time-step increases. The objective of this paper is to present an SPH technique that utilizes a projection method to model incompressible flows, and to investigate its efficiency and robustness compared to weakly compressible SPH. This SPH projection approach will be termed here "PSPH." The choices of time integration, projection operator, divergence, gradient, and viscous terms are described along with the treatment of boundary conditions and the numerical techniques used to solve the resulting elliptic problem. Numerical results for a vortex spin-down problem and a Rayleigh–Taylor instability are presented using both the projection method and the weakly compressible approach. A comparison of the total CPU times of the two techniques is also provided for the vortex spin-down. These results indicate that the proposed projection method is more robust and more efficient than the current weakly compressible approach.

2. SPH PROJECTION METHOD

2.1. Weakly Compressible SPH

In SPH the fluid is represented by a set of particles which follow the fluid motion and advect fluid quantities such as mass and momentum. In this Lagrangian framework, the Navier–Stokes equations are reduced to a set of ordinary differential equations at each particle. Smoothness and differentiability of the solution are achieved using an interpolation kernel W and summations over the particles b,

$$Q(\boldsymbol{r}) = \sum_b m_b \frac{Q_b}{\rho_b} W(|\boldsymbol{r} - \boldsymbol{r}_b|, h) \qquad \text{and} \qquad \nabla Q(\boldsymbol{r}) = \sum_b m_b \frac{Q_b}{\rho_b} \nabla W(|\boldsymbol{r} - \boldsymbol{r}_b|, h).$$

Here, h is the smoothing length, which in this paper is constant and is between 1 and 1.5 times the initial particle separation depending on the particular application. The mass, density, and position of particle b are m_b, ρ_b, and $\boldsymbol{r}_b$. There are a number of ways in which the Navier–Stokes equations can be represented in SPH (see [25]). The formulation implemented here is described by Monaghan [25] and represents the non-dimensional momentum equation at particle a as

$$\frac{d\boldsymbol{u}_a}{dt} = -\sum_b m_b \left[\left(\frac{P_b}{\rho_b^2} + \frac{P_a}{\rho_a^2} \right) \nabla_a W_{ab} + \chi_{ab} \right] + \frac{\boldsymbol{g}}{Fr^2}, \tag{1}$$

where P_b and $\boldsymbol{u}_b$ are the pressure and velocity at particle b. The pressure gradient term is designed to conserve total linear and total angular momentum [25]. The viscous stresses are χ_{ab}, $\boldsymbol{g}$ is a body force, and Fr is the Froude number. In this study the viscosity treatment proposed in [9] is used,

$$\chi_{ab} = -\frac{1}{Re}\frac{1}{\xi}\left(\frac{4}{\rho_a + \rho_b} \right) \frac{\boldsymbol{u}_{ab} \cdot \boldsymbol{r}_{ab}}{|\boldsymbol{r}_{ab}|^2 + \eta^2} \nabla_a W_{ab}, \tag{2}$$

where ξ is a calibration factor. In [9], $\xi = 0.2015$ in Couette flow simulations is used. However, comparisons between this viscosity treatment and that used in [27] to simulate low Re flows in SPH suggest that an appropriate value for the simulations presented in this paper is $\xi = 0.24$.

Density is evolved using the continuity equation

$$\frac{d\rho_a}{dt} = \sum_b m_b (\boldsymbol{u}_a - \boldsymbol{u}_b) \cdot \nabla_a W_{ab}. \tag{3}$$

In (1) to (3), $\boldsymbol{r}_{ab} = \boldsymbol{r}_a - \boldsymbol{r}_b$, $\boldsymbol{u}_{ab} = \boldsymbol{u}_a - \boldsymbol{u}_b$, and η is a small parameter included to ensure that the denominator remains nonzero. The notation W_{ab} is shorthand for

$$W_{ab} = W(\boldsymbol{r}_{ab}, h) = \frac{1}{h^\sigma} f\left(\frac{|\boldsymbol{r}_{ab}|}{h} \right), \tag{4}$$

where f is the interpolation kernel function and σ is the dimensionality of the problem. There are many choices for f and here, cubic or quartic spline kernel functions are used. The cubic kernel function (normalized for one dimension) is defined as

$$f(s) = \frac{2}{3} \begin{cases} 1.0 - 3s^2/2 + 3s^3/4, & 0 \le s < 1.0 \\ (2-s)^3/4, & 1.0 \le s < 2.0 \\ 0, & s \ge 2.0 \end{cases} \tag{5}$$

and is used to test the PSPH projection operator (see Section 2.3.2). The quartic spline kernel function (normalized for two dimensions) defined as

$$f(s) = 0.0255 \begin{cases} (2.5-s)^4 - 5(1.5-s)^4 + 10(0.5-s)^4, & 0 \le s < 0.5 \\ (2.5-s)^4 - 5(1.5-s)^4, & 0.5 \le s < 1.5 \\ (2.5-s)^4, & 1.5 \le s < 2.5 \\ 0, & s \ge 2.5 \end{cases} \tag{6}$$

is used for the simulations presented in Section 3.

In WCSPH simulations, the following equation of state [3] has been used [24],

$$P = \frac{c^2 \rho_0}{\Gamma}\left(\left(\frac{\rho}{\rho_0}\right)^{\Gamma} - 1\right), \tag{7}$$

where c is the sound speed, $\Gamma = 7$, and ρ_0 is the initial reference density. To approximate incompressibility, a large value of c is employed, typically resulting in a flow Mach number of $M \approx 0.1$. Because compressibility effects are $O(M^2)$, use of this Mach number, in theory, should result in maximum density variations of the order of 1%.

2.2. Time Integration

A first-order Euler time-step is employed in this study for ease of discussion, although higher order schemes are easily implemented. The particle positions, $\boldsymbol{r}_a^n$, are advected with velocity $\boldsymbol{u}_a^n$ to positions $\boldsymbol{r}_a^*$,

$$\boldsymbol{r}_a^* = \boldsymbol{r}_a^n + \Delta t\left(\boldsymbol{u}_a^n\right). \tag{8}$$

At these positions, an intermediate velocity field, $\boldsymbol{u}_a^*$, is calculated by integrating the SPH momentum equation forward in time without the pressure gradient term:

$$\boldsymbol{u}_a^* = \boldsymbol{u}_a^n - \Delta t\left(\sum_b m_b \chi_{ab}^n(\boldsymbol{r}^*) + \frac{\boldsymbol{g}}{Fr^2}\right). \tag{9}$$

The following pressure Poisson equation is then solved to obtain the pressure needed to enforce incompressibility:

$$\nabla \cdot \left(\frac{1}{\rho}\nabla P\right)_a = \frac{\nabla \cdot \boldsymbol{u}_a^*}{\Delta t}. \tag{10}$$

The pressure gradient is next added to obtain a divergent-free velocity field:

$$\boldsymbol{u}_a^{n+1} = \boldsymbol{u}_a^* - \Delta t \sum_b m_b \left(\frac{P_b}{\rho_b^2} + \frac{P_a}{\rho_a^2}\right)\nabla_a W_{ab}. \tag{11}$$

Finally, the particle positions are centered in time,

$$\boldsymbol{r}_a^{n+1} = \boldsymbol{r}_a^n + \Delta t\left(\frac{\boldsymbol{u}_a^{n+1} + \boldsymbol{u}_a^n}{2}\right). \tag{12}$$

The scheme is $O(\Delta t)$ because an explicit treatment of the viscous term is used and the projection is performed at particle positions $\boldsymbol{r}_a^*$ that are found from an $O(\Delta t)$ integration of $\boldsymbol{u}_a^n$. The intermediate velocity field $\boldsymbol{u}_a^*$ does not depend on the pressure gradient from the previous time-step. This type of projection is termed a *full pressure projection*. In contrast, an incremental pressure projection projects an intermediate velocity field that incorporates the pressure gradient from the previous time-step. Combining a full pressure projection with an approximate projection operator (see Section 2.3.2) has been shown to avoid error accumulation in grid-based methods [30], and was also found to give superior results with PSPH.

2.3. Pressure Projection

2.3.1. *Projection Fundamentals*

In a projection method, the pressure needed to enforce incompressibility is found by projecting an estimate of the velocity field onto a divergence-free space. The theory behind the projection approach is based on the Hodge decomposition which states that any vector field, $\mathbf{V}$, can be decomposed into a divergence-free component, $\mathbf{V}^{\mathrm{d}}$, and the gradient of some scalar, ϕ (a curl-free component). Thus,

$$\mathbf{V} = \mathbf{V}^{\mathrm{d}} + \nabla\phi. \tag{13}$$

The projection operator, $\mathbf{P}$, for a variable density flow is [5]

$$\mathbf{P} = \mathbf{I} - \sigma\mathbf{G}(D\sigma\mathbf{G})^{-1}D, \tag{14}$$

where D is a divergence operator, $\mathbf{G}$ is a gradient operator, and $\sigma = \frac{1}{\rho}$. The projection $\mathbf{P}$ will project any vector $\boldsymbol{u}^*$ onto the space of divergence-free vector fields provided $D = -(\sigma\mathbf{G})^T$. Typically, $\boldsymbol{u}^*$ is an intermediate estimate of the velocity field obtained from updating the momentum equations either by using a time-lagged pressure gradient or by neglecting the pressure gradient altogether.

In the majority of projection techniques, the Hodge decomposition is undertaken by solving for the curl-free component, $\nabla\phi$, and subtracting it from the original vector $\boldsymbol{u}^*$. This is achieved by solving the pressure Poisson equation (PPE)

$$D\sigma\mathbf{G}P = \frac{D\boldsymbol{u}^*}{\Delta t} \tag{15}$$

for the pressure P and subtracting $\Delta t\sigma\mathbf{G}P$ from $\boldsymbol{u}^*$ to give the incompressible velocity field $\boldsymbol{u}^{n+1}$:

$$\boldsymbol{u}^{n+1} = \boldsymbol{u}^* - \Delta t(\sigma\mathbf{G}P). \tag{16}$$

2.3.2. *An SPH Projection Operator*

There are a number of different grid-based projection algorithms discussed and analyzed in the literature (e.g., [30]). Either an exact projection or an approximate projection can be used. An exact projection operator is constructed by ensuring that the divergence and gradient operators are discretely skew adjoint, i.e., $D = -(\sigma\mathbf{G})^T$. It can be shown that the SPH divergence operator defined by

$$\nabla\cdot\boldsymbol{u}_a = \rho_a\sum_b m_b\left(\frac{\boldsymbol{u}_b}{\rho_b^2} + \frac{\boldsymbol{u}_a}{\rho_a^2}\right)\cdot\nabla_a W_{ab} \tag{17}$$

is skew adjoint to the gradient operator used in (1) when the density is constant. Employing these adjoint SPH divergence and gradient operators at constant density leads to the pressure Poisson equation

$$(D\mathbf{G})P_i = \sum_j \frac{m_j}{\rho_j}\left(\sum_l \frac{m_l}{\rho_l}P_l\nabla_j W_{lj}\right)\cdot\nabla_i W_{ij} = \frac{D\boldsymbol{u}_i^*}{\Delta t}. \tag{18}$$

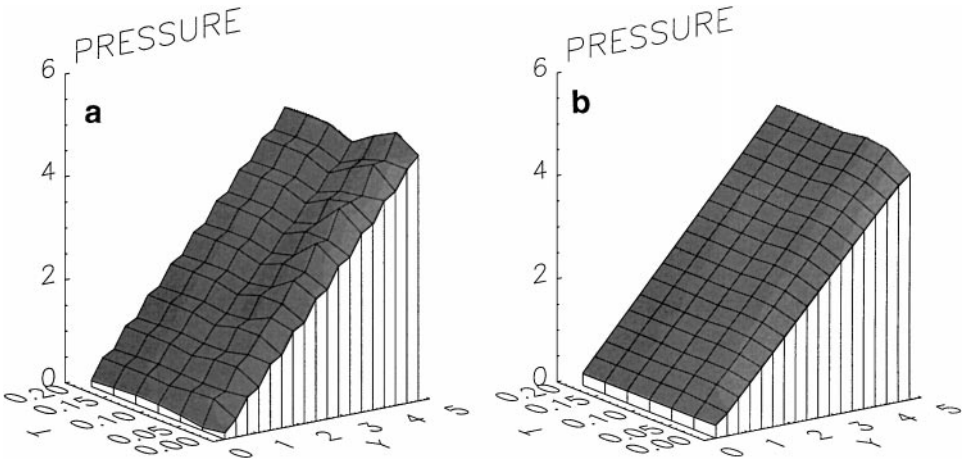

FIG. 1. P vs y and t using a cubic spline kernel, $h = 1.4\Delta x$, $N = 20$. (a) Exact projection operator. (b) Approximate projection operator. Note the pressure decoupling using the exact projection operator.

This exact projection was tested on a simple one-dimensional hydrostatic equilibrium problem, using the cubic spline kernel given in (5) with $h = 1.4\Delta x$. The results are shown in Fig. 1a. The exact projection operator produces a distinct pressure decoupling pattern similar to that observed in exact projection methods on co-located finite-difference grids [31]. Analogous problems have also occurred with equal-order interpolation elements in finite-element methods [32]. This type of problem also hampers convergence when iterative techniques are used to perform the projection.

Approximate projection methods were introduced (for example, [30]) in grid-based methods to avoid these decoupling problems. Unlike exact projection methods, the divergence and gradient operators are not discretely skew adjoint but are chosen so that the Laplacian operator, $L = D\sigma\mathbf{G}$, is easily discretized. For example, on a two-dimensional co-located finite difference grid, the approximate projection operator is usually written as a five-point Laplacian stencil whereas the exact projection, $L = D\sigma\mathbf{G}$, results in four sets of decoupled five-point stencils [30].

In this paper, an approximate projection is used which utilizes the following SPH stencil for the PPE operator in (10),

$$L(P_a) = D\sigma\mathbf{G}(P_a) = \sum_b \frac{m_b}{\rho_b}\left(\frac{4}{\rho_a + \rho_b}\right)\frac{P_{ab}\,\boldsymbol{r}_{ab}\cdot\nabla_a W_{ab}}{|\boldsymbol{r}_{ab}^2| + \eta^2}, \tag{19}$$

where $P_{ab} = P_a - P_b$. This is analogous to the approximation used in [22] for thermal diffusion and also for the viscous diffusion term in (2). The approximate projection operator was tested on the same one-dimensional hydrostatic equilibrium problem and the results are shown in Fig. 1b. It prevents the pressure decoupling that arises when an exact projection is used.

2.4. Solvability and the PPE Source Term

Because the pressure Poisson equation (10) employs Neumann boundary conditions for P, a compatibility constraint must be satisfied in order for (10) to have a unique solution. This constraint relates the source of the Poisson equation to the Neumann boundary conditions

through the divergence theorem,

$$\int_V \nabla \cdot \left(\frac{1}{\rho}\nabla P\right) dV = \int_V \frac{\nabla \cdot \boldsymbol{u}^*}{\Delta t}\, dV = \int_\Gamma \boldsymbol{n} \cdot \boldsymbol{u}^*\, dS = 0, \tag{20}$$

provided $\boldsymbol{u}^*$ satisfies the correct boundary conditions.

This implies that each time (10) is solved, the total sum of the discrete source terms ($\sum_{i=1}^{N} \nabla \cdot \boldsymbol{u}_i^*$) must be zero. In matrix form, the solution of the system

$$A\boldsymbol{P} = \boldsymbol{b}, \tag{21}$$

where $A = L = D\sigma\mathbf{G}$ (symmetric) and $\boldsymbol{b} = D\boldsymbol{u}^*/\Delta t$ requires $\boldsymbol{b}$ to be in the column space of A, i.e., $\boldsymbol{b} \in R(A)$. Since A is constructed by using homogeneous Neumann boundary conditions for the pressure, there exists a constant vector, $\boldsymbol{c}$, in the left null space of A, i.e., $A\boldsymbol{c} = \mathbf{0} = A^T\boldsymbol{c} = \boldsymbol{c}^T A$. Multiplying (21) by $\boldsymbol{c}^T$ gives the constraint

$$\boldsymbol{c}^T\boldsymbol{b} = 0, \tag{22}$$

which again implies that in discrete form, the sum of the source terms is

$$\sum_{i=1}^{N} \nabla \cdot \boldsymbol{u}_i^* = 0. \tag{23}$$

On a finite-difference MAC grid, this solvability constraint is automatically satisfied for Neumann velocity boundary conditions. However on other grids, additional measures are required to satisfy it. For example, in [6, 33] solvability on a co-located grid was satisfied by subtracting the mean value of the source term from each local discrete source while in [1], the PPE was written in conservative form.

In PSPH, the solvability constraint is satisfied by employing the divergence operator given by (17) (assuming $m_a/\rho_a = m_b/\rho_b$). This expression is analogous to the pressure gradient term in (1). Whereas the pressure gradient term in (1) conserves total momentum, the divergence term in (17) conserves total mass.

2.4.1. *Elliptic Solvers*

There are many different techniques that can be used to solve (10). Here, two methods are considered: a defect correction multi-grid method; and a conjugate gradient method with a diagonal pre-conditioner. The multi-grid method was implemented in a spirit similar to that in [26], where it was used to solve for the gravitational potential in interstellar cloud simulations. Unlike in [26], the Poisson equation is satisfied on the particles rather than on the underlying grid. This is done by treating the particles as the finest level grid. Coarse level grids are uniform rectangular grids, each of which has twice the grid spacing of the next finer grid. The first coarse mesh has a grid spacing of $2.5h \times 2.5h$. At the particle level and all coarser levels, Gauss–Seidel relaxation is applied and the error restricted to the next level grid using the quartic spline kernel given by (6). At coarse levels, a standard defect correction multi-grid technique is used, with the correction prolonged to finer grids using a bilinear interpolation. Bilinear interpolation is also used to prolong the correction to the particles. To avoid large memory requirements, the matrix $A = L = D\sigma\mathbf{G}$ for the particle level Gauss–Seidel and conjugate gradient iterations is stored in sparse form.

2.5. Boundary Conditions

Two issues arise in the implementation of boundary conditions in the PSPH technique. The first issue is the choice of appropriate boundary conditions and the second issue is the method of application of these conditions. Homogeneous Neumann boundary conditions are used for the pressure in (10) and the Dirichlet conditions $\boldsymbol{u}^* = \boldsymbol{w}$ and $\boldsymbol{u}^{n+1} = \boldsymbol{w}$ are enforced on solid boundaries ($\boldsymbol{w}$ is the prescribed boundary velocity). These boundary conditions do not satisfy the correct pressure boundary conditions required for the incompressible Navier–Stokes equations [15]; however, they have been shown to work well in practice when combined with projection methods [14]. These conditions are implemented here using external, fictitious particles whose positions are defined by reflecting the interior fluid particles across the boundary position. The effect of these fictitious particles is implicitly included in the summations for the gradient, projection, and viscous operators in the following way. Referring to Fig. 2a, for a given particle pair interaction, $a \to b$, an

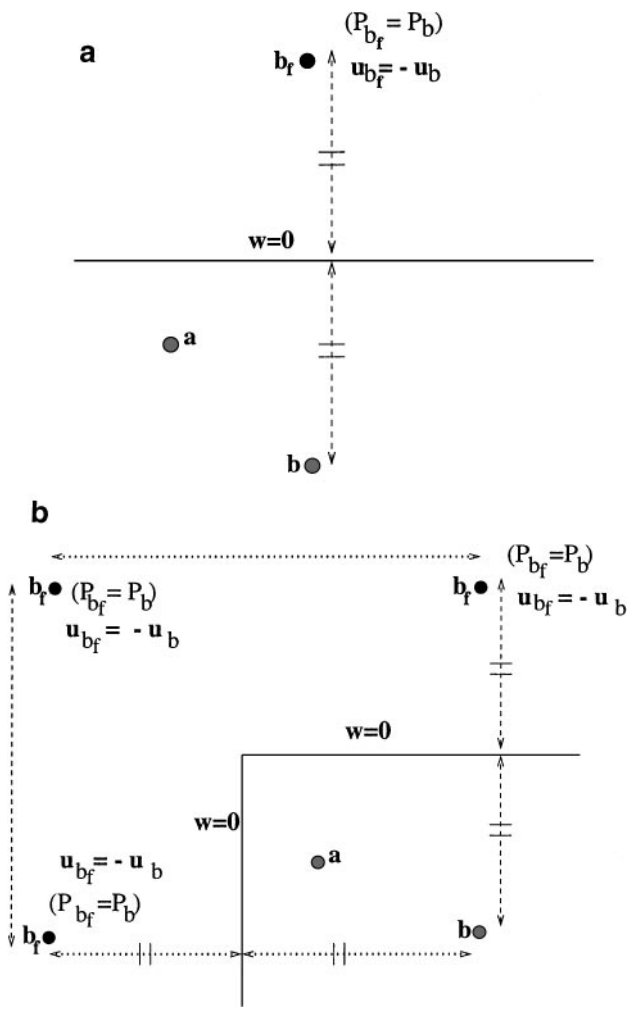

FIG. 2. Boundary treatment. (a) For a particle b near an edge interacting with a particle a an additional interaction needs to take place between particles a and b_f. b_f is a fictitious particle that can be considered a reflection of b across the boundaries. (b) For a particle b near a corner interacting with a particle a, three additional interactions need to take place between particle a and the three reflected particles b_f.

additional interaction $a \rightarrow b_f$ is included in the summation. The fictitious particle b_f has the following properties:

- Position—$\boldsymbol{r}_{b_f}$ is found by a direct reflection of particle b across the boundary line. The position of particle b_f therefore mirrors that of b.
- Velocity—For the wall-bounded simulations in this paper, no slip velocity conditions $\boldsymbol{u}^*_{b_f} = 2\boldsymbol{w} - \boldsymbol{u}^*_b$ and $\boldsymbol{u}^{n+1}_{b_f} = 2\boldsymbol{w} - \boldsymbol{u}^{n+1}_b$ are employed. This is a linear extrapolation of the interior and boundary velocities to obtain the external velocity. It is similar to the technique used in finite-difference methods. In this way, $\boldsymbol{u}^*_{int} = \boldsymbol{w}$ and $\boldsymbol{u}^{n+1}_{int} = \boldsymbol{w}$ is ensured at any point along the boundary ($\boldsymbol{u}_{int}$ is a velocity along the boundary that would result from interpolating the surrounding internal and assigned external particle velocities). This is important for obtaining an accurate representation of the viscous operator associated with particle a when a is near the boundary. When a is on the boundary, $\boldsymbol{u}^*_a = \boldsymbol{w}$ and $\boldsymbol{u}^{n+1}_a = \boldsymbol{w}$ is set and evaluation of the viscous term at a is not required.
- Pressure—$P_{b_f} = P_b$. In this way, homogeneous Neumann boundary conditions $\frac{\partial P}{\partial n} = 0$ are enforced along the boundary line. This is important for obtaining an accurate representation of the projection and gradient operators associated with particle a when a is near or on the boundary. When a is on the boundary, P_a is found by solving (10) with $\nabla \cdot \boldsymbol{u}^*_a / \Delta t = 0$. Setting $\nabla \cdot \boldsymbol{u}^*_a / \Delta t = 0$ on the boundary is correct as long as $\mathbf{n} \cdot (\boldsymbol{u}^* - \boldsymbol{w}) = 0$ (see [15]), which is consistent with the velocity boundary conditions applied here.

Figure 2b shows how this boundary treatment is generalized for corners.

Unlike the gradient, projection, and viscous operators, the effect of these fictitious particles is not included in the summations for the divergence operator. This choice was made to ensure that the solvability constraint (23) is automatically satisfied. It is possible to implicitly include these fictitious particles in the summations for the divergence operator, but additional measures would then be required to satisfy solvability.

3. SIMULATIONS

To assess the accuracy and efficiency of the PSPH method, two problems (a two-dimensional vortex spin-down and a Rayleigh–Taylor instability) are calculated using

1. an exact projection method performed on a staggered finite-difference MAC grid [11];
2. the PSPH technique described in this paper with the quartic spline kernel (6) with smoothing length $h = 1.3\Delta x$ (where Δx is the initial particle spacing); and
3. the WCSPH technique with the quartic spline kernel with smoothing length $h = 1.3\Delta x$ and an equation of state given by (7).

For both PSPH and WCSPH, a quantitative measure of incompressibility is provided for PSPH and WCSPH by evaluating the coefficient of variation of number density, $CV(t)$, as a function of time t. It is a measure of the average variation of number density, at each particle normalized with respect to the average number density, and is given by

$$CV(t) = \frac{\sqrt{\frac{1}{N}\sum_{i=1}^{N}(d_i(t) - d_i(0))^2}}{\frac{1}{N}\sum_{i=1}^{N}\frac{d_i(t)}{d_i(0)}}, \tag{24}$$

where the number density at particle a, d_a, is the interpolant of $(\rho/m)_a$ and is estimated

using

$$d_a = \sum_{b=1}^{N} W_{ab}. \tag{25}$$

In an ideal incompressible SPH, particles would be advected to positions such that $CV(t) = 0$ for all times t.

3.1. Vortex Spin-down

A two-dimensional vortex spin-down at $Re = 420$ is calculated, with $\rho = 1$, $\boldsymbol{g} = \mathbf{0}$, and an initial velocity field given by

$$\begin{aligned} u &= 0.25(y - 0.5) \\ v &= 0.25(0.5 - x) \end{aligned} \tag{26}$$

in a unit square with boundary conditions $\boldsymbol{w} = \mathbf{0}$. The simulation was run from time $t = 0$ to 10 using an exact projection on a staggered finite-difference MAC grid, the PSPH technique, and the WCSPH technique with the following specifications:

1. exact projection $\Rightarrow$ 128×128 grid;
2. PSPH method $\Rightarrow$ 50×50 particle lattice;
3. WCSPH method $\Rightarrow$ 50×50 particle lattice with sound speed $c = 1.25$ using Lennard-Jones type boundary forces (see Section 3.1.1).

The exact projection case is performed at a higher resolution to provide a close-to-"exact" solution, from which both SPH techniques can be compared.

3.1.1. *Optimal WCSPH Solution*

As the choice of sound speed and boundary conditions can significantly affect the results of a compressible SPH simulation, six WCSPH simulations were calculated for this problem from which the best solution was chosen. In the first three simulations, the boundary conditions outlined in Section 2.5 (termed here as "PSPH boundary conditions") were employed with sound speeds $c = 5.00$, $c = 2.50$, and $c = 1.25$. Figure 3 shows the decay of the maximum velocity magnitude (normalized with respect to the initial maximum velocity magnitude) with time resulting from these three simulations. The remaining three simulations were performed using the same three sound speeds with boundary particles exerting Lennard-Jones type forces on fluid particles described in [24]. Figure 4 reveals the corresponding velocity decay graphs. All six simulations show large oscillations up to time $t = 2.0$ which decay as the maximum velocity decays. For both boundary conditions, the use of $c = 5.00$ leads to a noticeably faster decay rate than the use of $c = 1.25$ and $c = 2.50$ and oscillations near time $t = 9.0$. Further investigation of these oscillations reveals that they also occur for $c = 2.50$ and $c = 1.25$ at later times (at time $t = 12.0$ for $c = 2.50$ and at time $t = 16.0$ for $c = 1.25$) and eventually lead to instabilities. Animations of the spin-down velocity field show that the wavelength of the oscillation is large relative to the particle spacing, indicating that it is a result of sound wave propagation rather than a short wavelength tensile instability discussed in [28]. Cleary [10] has reported similar sound wave propagations when simulating hydrostatic equilibrium using WCSPH. No such instabilities were noted for the PSPH method.

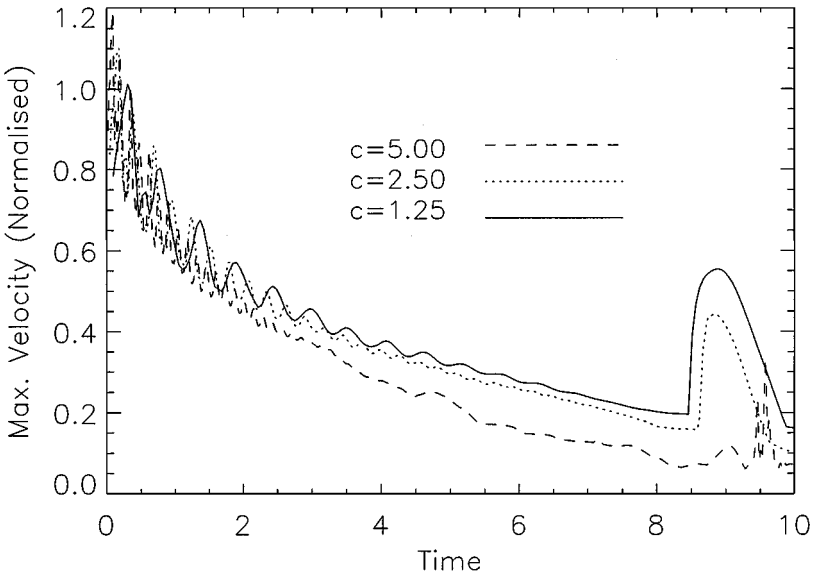

FIG. 3. Vortex spin-down velocity decay using WCSPH with sound speeds $c = 1.25$, $c = 2.50$, and $c = 5.00$ with PSPH boundary conditions.

The results for $c = 1.25$ and $c = 2.50$ using PSPH boundary conditions shown in Fig. 3 display a large anomalous jump in maximum velocity at time $t = 8.50$ which is not observed for $c = 5.00$. Analysis of the particle velocities at this time reveals that these velocities occur at particles close to the boundary which are repelled from the boundary because of the PSPH boundary conditions. These anomalies were not observed when Lennard-Jones type

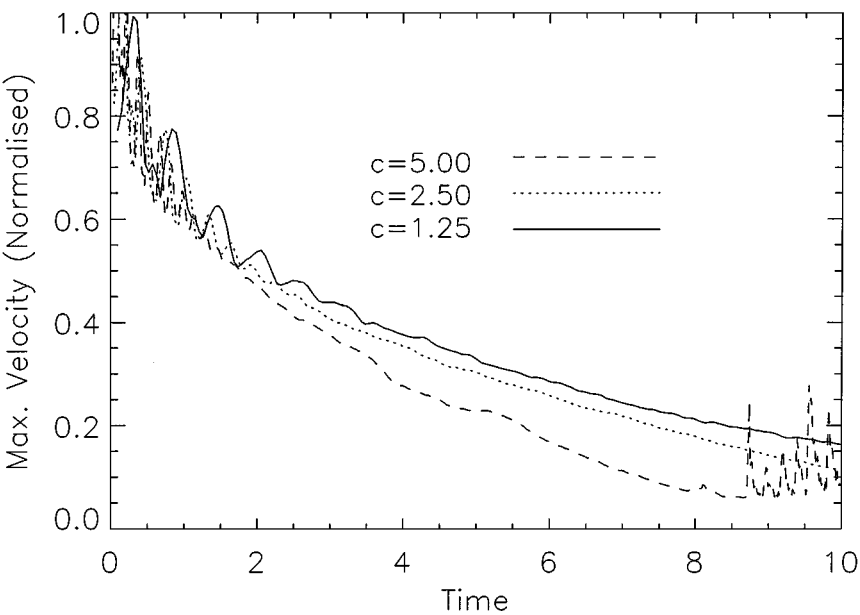

FIG. 4. Vortex spin-down velocity decay using WCSPH with sound speeds $c = 1.25$, $c = 2.50$, and $c = 5.00$ with Lennard-Jones type boundary forces.

boundary forces were used because these forces prevent particles from getting too close to the boundary.

This exercise highlights a major disadvantage of WCSPH—the need to refine results to ensure that an appropriate combination of sound speed and boundary conditions is used to give the most accurate solution. No such refinement was required for PSPH. Of the six tests performed, the simulation using $c = 1.25$ with Lennard-Jones type boundary forces provided the best comparison to the exact projection velocity solution and is used as the optimum WCSPH result in comparisons with PSPH and the exact projection technique.

3.1.2. *Results*

Figure 5 shows the streamlines and velocity vectors at $t = 8$ for the exact projection, PSPH, and WCSPH. The PSPH technique compares favorably with the finite-difference exact projection technique but the WCSPH result not only exhibits noise (due to the continued propagation and reflection of the sound waves off the solid boundaries) but also experiences an increase in the effective viscosity of the flow. This increase in effective viscosity for WCSPH is also seen in Fig. 7, which shows the decay of the maximum velocity magnitude with time for all three techniques. The PSPH results compare well to the finite-difference exact projection results throughout the entire simulation while the WCSPH technique gives rise to a faster decay.

Figure 8 show the variation of CV with time for the two SPH methods. Results from PSPH show a slow accumulation of density variation, with CV climbing steadily to 0.015 at $t = 10$. After this time, the rate of increase in CV significantly reduces; by time $t = 15$ it rises only to 0.016. (This is not entirely unexpected as the velocities and hence particle motion have reduced significantly after time $t = 10$.) Results from the WCSPH technique initially rise rapidly to $CV = 0.015$ and then stabilize at approximately $CV = 0.009$, remaining almost constant after this time. The particle positions at $t = 10$ shown in Fig. 6 provide insight into the behaviour of CV shown in Fig. 8. Slight gaps are visible in the particle positions resulting from PSPH. These gaps gradually appear as the simulation progresses and are a result of the fact that the shear field repeatedly compresses the flow in one direction and extends it in another. In the WCSPH technique, a line of particles forms along the boundary which is related to the use of boundary forces. This lining of particles occurs early in the simulation ($t < 1$) and is the probable cause of the sudden rise in CV early in the simulation.

The PSPH technique provides more accurate results for the velocity fields; it does, however, accumulate more error in local density (as seen by the CV comparisons in Fig. 8). (Similar results were noted for this particular problem when run with doubly periodic boundary conditions rather than solid wall boundaries. The WCSPH technique again produced a larger velocity decay rate relative to the PSPH and exact projection methods and oscillations toward the end of the simulation, but a smaller CV value. The PSPH method produced $CV = 0.024$ by time $t = 15.0$ compared to $CV = 0.005$ for WCSPH.) This accumulation in local density error for the PSPH technique is not surprising since, for any projection method, the resulting velocity $\boldsymbol{u}^{n+1}$ is divergence free only to within a spatial truncation error. Hence, errors in particle positions will result in density errors. Subsequent projections are therefore performed at incorrect particle positions, causing further error accumulation. Similar error accumulation occurs in vortex methods [29] and particle-in-cell methods [19], which can be remedied by the use of rezoning techniques.

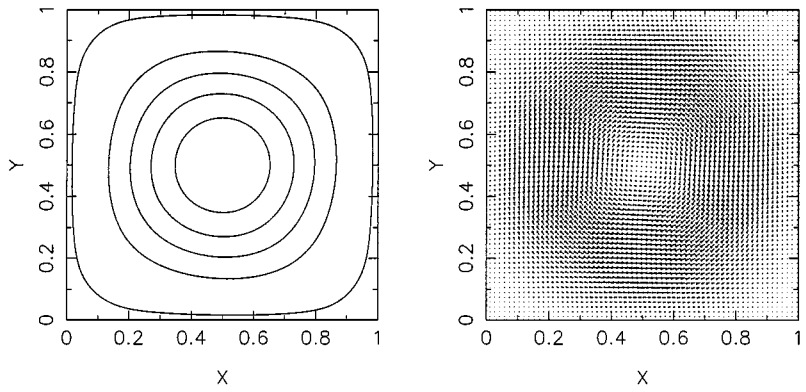

(i) Exact Projection

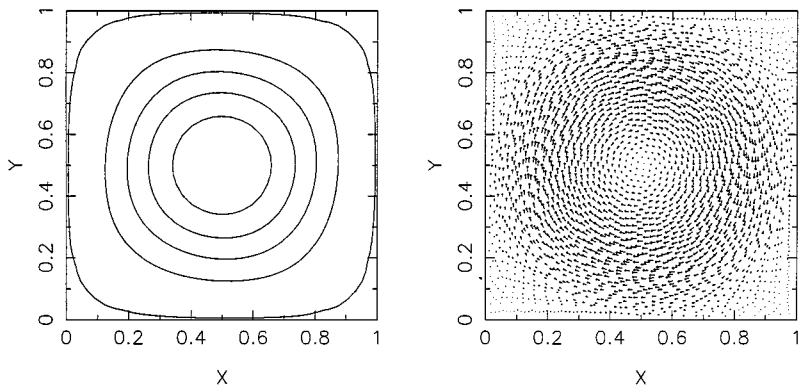

(ii) PSPH Method

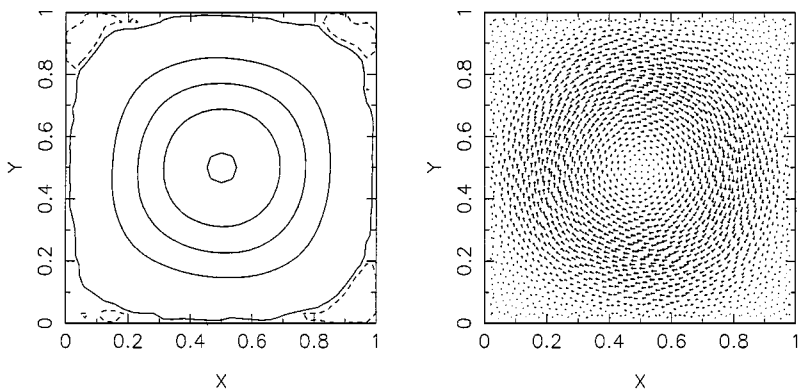

(iii) WCSPH Method

FIG. 5. Vortex spin-down streamlines and velocity vectors at time $t = 8$.

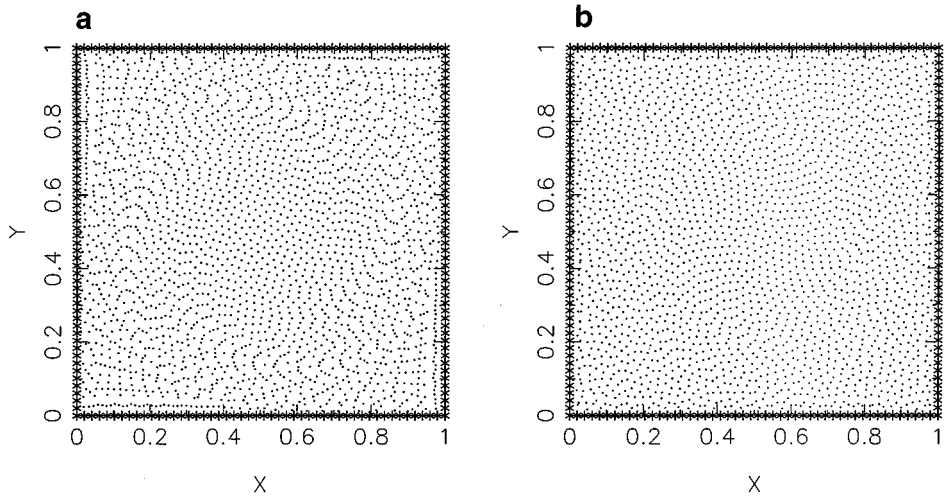

FIG. 6. Vortex spin-down particle positions at time $t = 10$. (a) PSPH method. (b) WCSPH method.

3.2. Rayleigh–Taylor Instability

The vortex spin-down problem does not utilize the natural advantages that Lagrangian SPH methods have over grid-based methods. A more appropriate test case of the PSPH method is the Rayleigh–Taylor instability in which the location of two different fluids and the interface that separates them must be accurately followed. This phenomenon occurs in a multitude of physical and industrial applications.

The initial conditions and specifications of the instability are given in Fig. 9. In this paper, the different fluid densities were set by using particles with different masses but the same

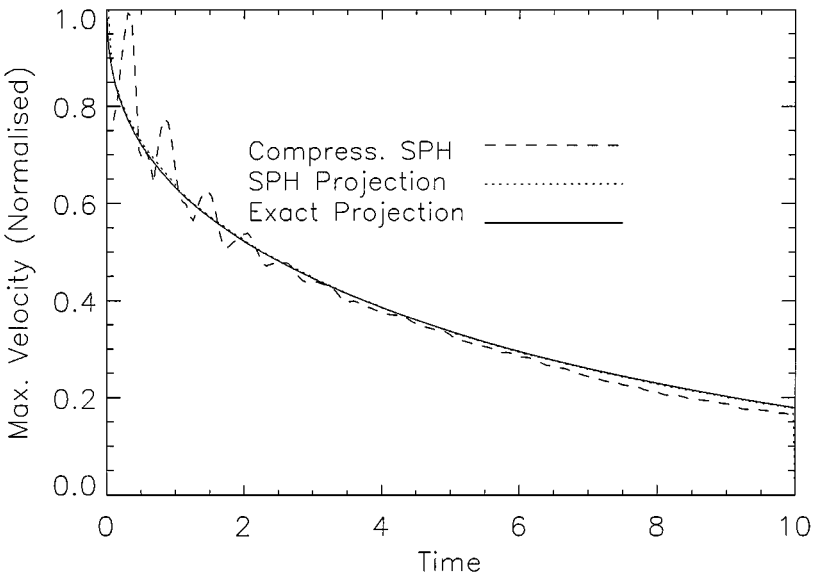

FIG. 7. Vortex spin-down velocity decay using PSPH (denoted as SPH Projection), WCSPH (with Lennard-Jones type boundary forces and $c = 1.25$, denoted as Compress. SPH), and the Exact Projection.

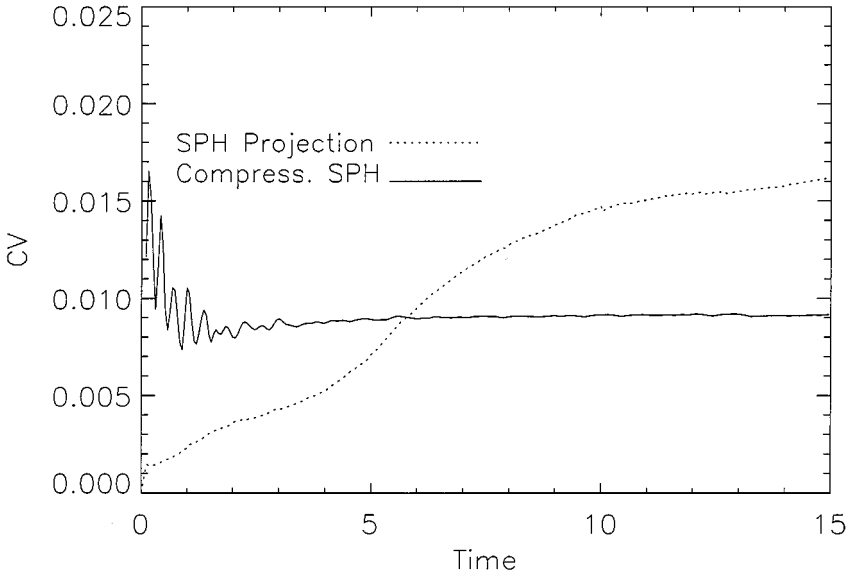

FIG. 8. Vortex spin-down *CV* for PSPH (denoted as SPH Projection) and WCSPH (denoted as Compress. SPH).

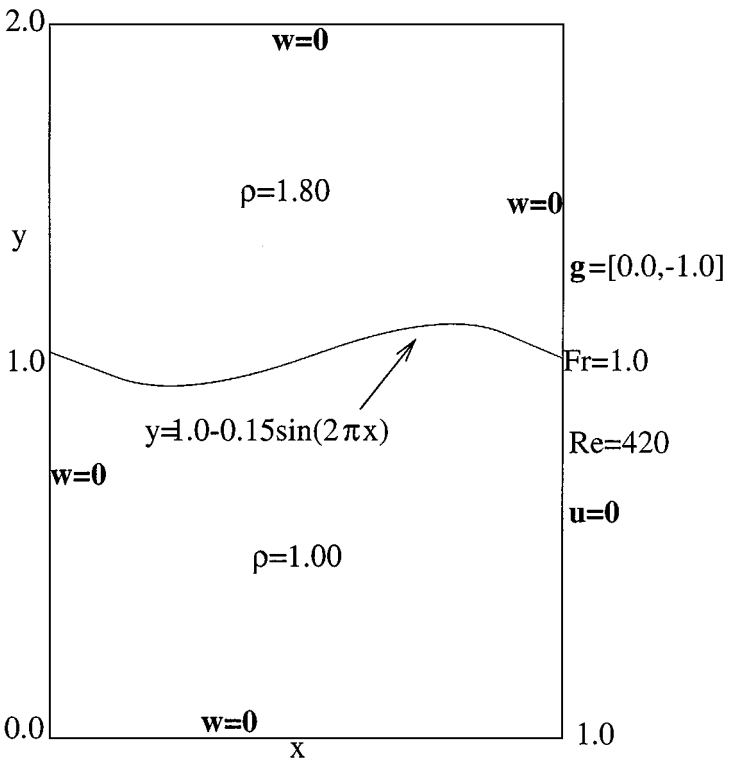

FIG. 9. Initial conditions and specifications of the Rayleigh–Taylor instability.

number density, although this is not the only way to achieve different densities in SPH. The simulation was performed using

1. exact projection $\Rightarrow 16 \times 32$ staggered MAC grid (using a volume tracking method to track the interface) [11];
2. PSPH method $\Rightarrow 53 \times 105$ particle lattice;
3. WCSPH method $\Rightarrow 53 \times 105$ particle lattice with sound speed $c = 10\sqrt{(|\mathbf{g}|H)} = 14.14$ [24], where $H = 2$ is the maximum height with Lennard-Jones type boundary forces employed.

Unlike the vortex spin-down, where increased resolution does not result in finer scales of motion (just smoother and more accurate results), numerical simulation of the Rayleigh–Taylor instability keeps on producing finer scales of density stratification until the resolution of the method is reached. When comparing the results for this problem, it is important to ensure that the resolution of the SPH and finite difference methods are equivalent. In a typical finite-difference simulation, the effective resolution scales with grid size Δx_{FD}. In a typical SPH simulation, however, the effective resolution scales with the smoothing distance of the kernel ($2.5h$ when using the quartic spline kernel given by (6)). For a 53×105 SPH particle lattice using the quartic spline kernel and $h = 1.3\Delta x$, the equivalent finite-difference resolution is approximately a 16×32 grid.

The interface positions at times $t = 3$ and $t = 5$ for each method are shown in Figs. 10 and 11 and the streamlines at $t = 5$ are shown in Fig. 12. The results for PSPH are closer to the results from the exact projection in both the interface position and streamlines with more fine scale structure predicted. However, by time $t = 5$, the plume is beginning to roll up in the finite-difference simulation, but not in either of the SPH simulations.

This highlights a tendency for particles in some SPH simulations to "clump" together near interfaces of different materials, producing an artificial surface tension that prevents regions of high curvature from forming. This particle clumping is illustrated in Fig. 13, which shows a plot of the particles near the interface at time $t = 3$. Hoover [16] has also

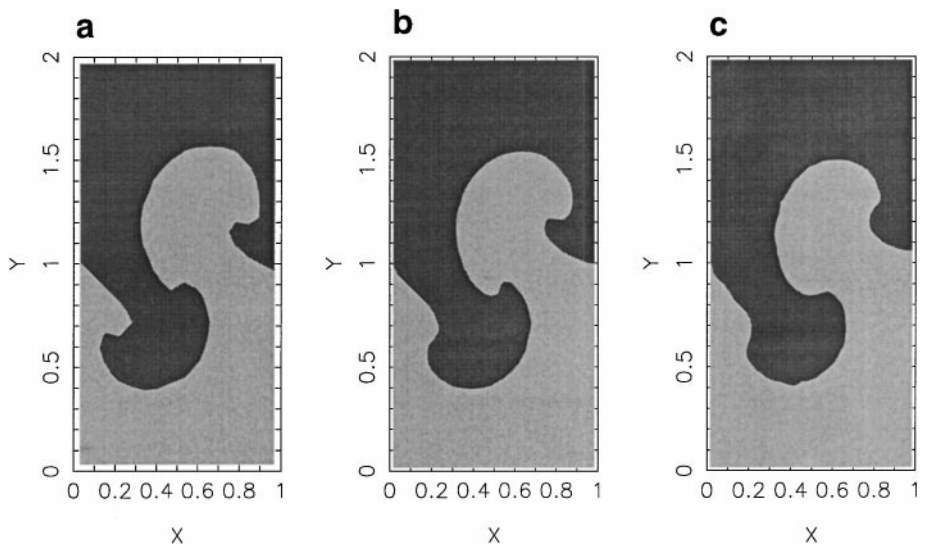

FIG. 10. Interface positions at time $t = 3$ for the Rayleigh–Taylor instability using (a) Exact Projection, (b) PSPH, (c) WCSPH.

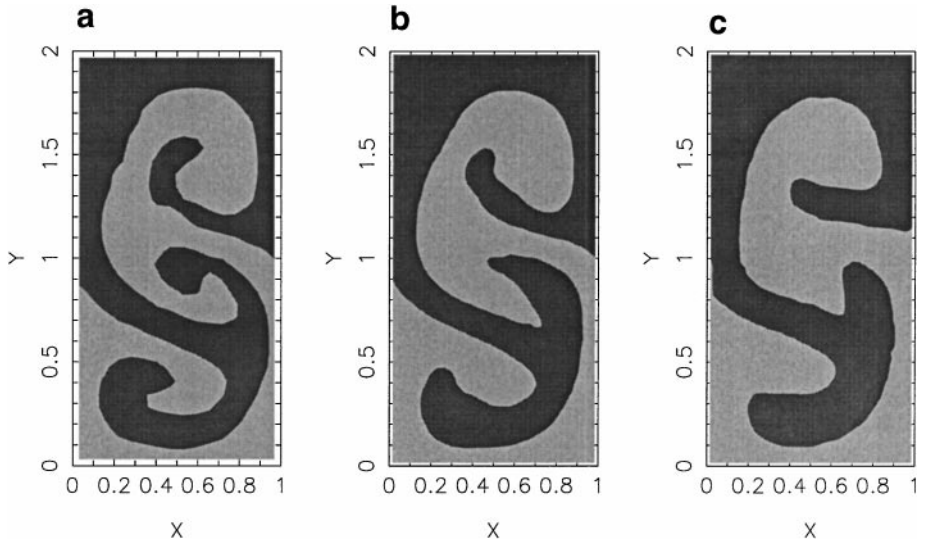

FIG. 11. Interface positions at time $t = 5$ for the Rayleigh–Taylor instability using (a) Exact Projection, (b) PSPH, (c) WCSPH.

noted this artificial surface tension in SPH and attributes it to the properties of the pressure gradient operator used in this paper (see (1)). Both the divergence and gradient operators (see (1) and (17)) are formulated assuming a differentiable density field and large density discontinuities (such as those found at a fluid–fluid interface) cannot be accurately modeled using these operators.

In Fig. 14, *CV* is plotted for PSPH and WCSPH. Like the use of the vortex spin-down, the use of the PSPH method results in a slow accumulation of density variation with *CV* climbing steadily to 0.011 at $t = 15$. The WCSPH technique, in contrast, produces a large density variation error, with *CV* rising continually to approximately 0.052 by $t = 7$ and then

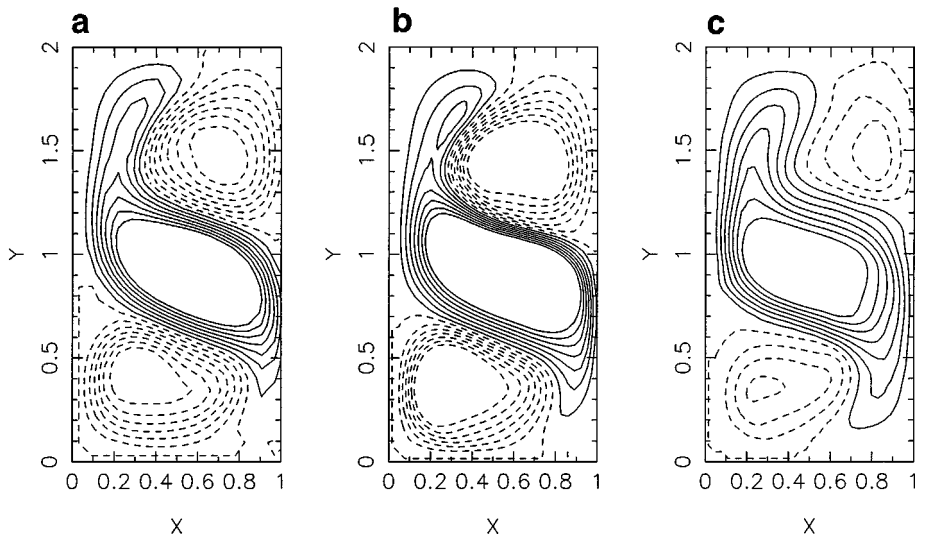

FIG. 12. Streamlines at time $t = 5$ for the Rayleigh–Taylor instability using (a) Exact Projection, (b) PSPH, (c) WCSPH.

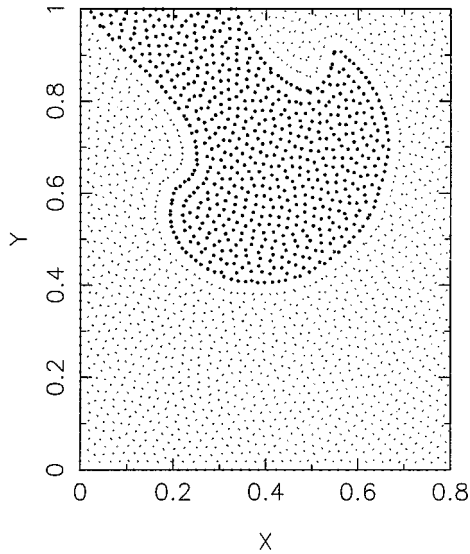

FIG. 13. Particle positions at time $t = 3$ for the Rayleigh–Taylor instability using PSPH.

remaining approximately constant after this. This behavior is markedly different from that produced by the vortex spin-down, which displayed an initial sharp rise in *CV* that leveled off to 0.012. In terms of local density conservation, PSPH has performed far better than WCSPH for this Rayleigh–Taylor instability.

To ensure that the most appropriate combination of sound speed and boundary conditions was chosen, the simulation was also run with sound speeds $c = 20\sqrt{(|\mathbf{g}|H)}$ and $c = 5\sqrt{(|\mathbf{g}|H)}$ using the Lennard-Jones boundary forces and sound speeds $c = 20\sqrt{(|\mathbf{g}|H)}$, $c = 10\sqrt{(|\mathbf{g}|H)}$, and $c = 5\sqrt{(|\mathbf{g}|H)}$ using PSPH boundary conditions. Using the

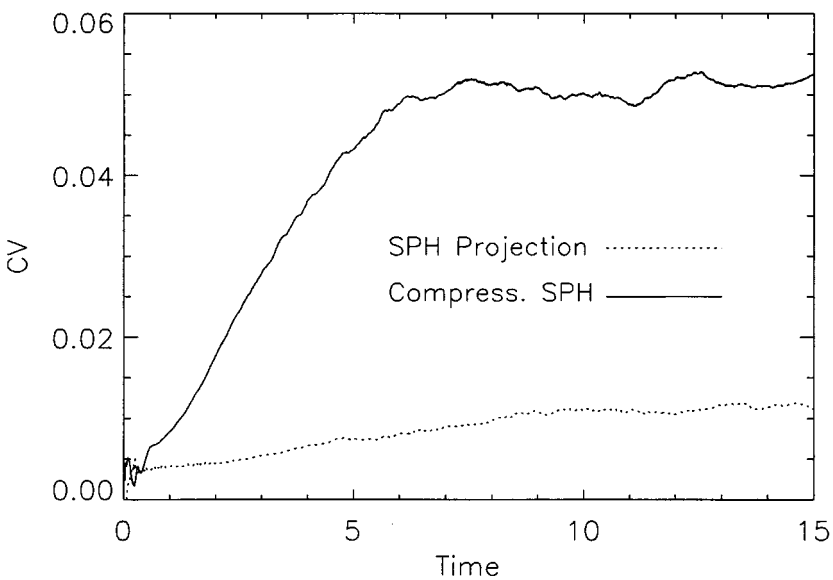

FIG. 14. Rayleigh–Taylor instability *CV* for PSPH (denoted as SPH Projection) and WCSPH (denoted as Compress. SPH) .

Lennard-Jones boundary forces, rather than PSPH boundary conditions, resulted in more stable and robust solutions for all sound speeds. Combining these boundary conditions with sound speed $c = 20\sqrt{(|\mathbf{g}|H)}$ reduced the density error, producing $CV = 0.048$ by time $t = 15.0$, but gave poorer velocity comparisons. In contrast, using $c = 5\sqrt{(|\mathbf{g}|H)}$ produced more comparable velocity fields but larger density errors, with $CV = 0.062$ by time $t = 15.0$. Thus, the use of all three sound speeds in WCSPH still produces CV values significantly larger than those produced by PSPH for the Rayleigh–Taylor instability. It is interesting to note that the vortex spin-down problem produced a larger CV value using PSPH ($CV = 0.016$ by time $t = 15.0$) than did the Rayleigh–Taylor instability ($CV = 0.011$ by time $t = 15.0$), despite the larger displacement of particles in the Rayleigh–Taylor problem. This is probably due to the more repetitive nature of the spin-down problem, which repeatedly stretches the flow in the same direction.

3.3. Efficiency

The efficiency of the PSPH method was estimated by measuring the total CPU times required to run the vortex spin-down problem to time $t = 0.5$ using:

1. WCSPH method (Compr.);
2. PSPH method, using multi-grid to solve (10) (MG);
3. PSPH method, using a conjugate gradient method with a diagonal pre-conditioner to solve (10) (CGPD).

The Reynolds number was set at 420 and grid resolutions ranging from 27×27 to 105×105 were considered. The simulations were run on an R10000 SGI Power Challenge.

For the PSPH method at $Re = 420$, the time-step is governed by the CFL stability constraint

$$\Delta t \leq \frac{0.25h}{|\boldsymbol{u}|_{\max}} \tag{27}$$

for resolutions less than 50×50. For higher resolutions, the viscous diffusion condition

$$\Delta t \leq 0.125\,\mathrm{Re}\,h^2 \tag{28}$$

is the dominant time-step constraint, where (28) is based on the Fourier stability analysis for a finite-difference method on a uniform mesh.

For the WCSPH technique at $Re = 420$, Δt is governed by the CFL stability constraint

$$\Delta t \leq \frac{0.25h}{c} \tag{29}$$

(where the sound speed $c = 1.25$) for all resolutions.

Figure 15 provides the efficiency comparison results. The multi-grid projection is always more efficient than the weakly compressible technique, particularly so at the lower and medium resolutions where the CFL condition governs. However, as the resolution increases and the time-step constraint becomes more severe for the projection techniques (i.e., $\Delta t \propto h^2$ due to the viscous diffusion condition), the time taken for the multi-grid projection approaches the weakly compressible time. The conjugate gradient technique is also more efficient than the weakly compressible SPH but only for resolutions less than 80×80.

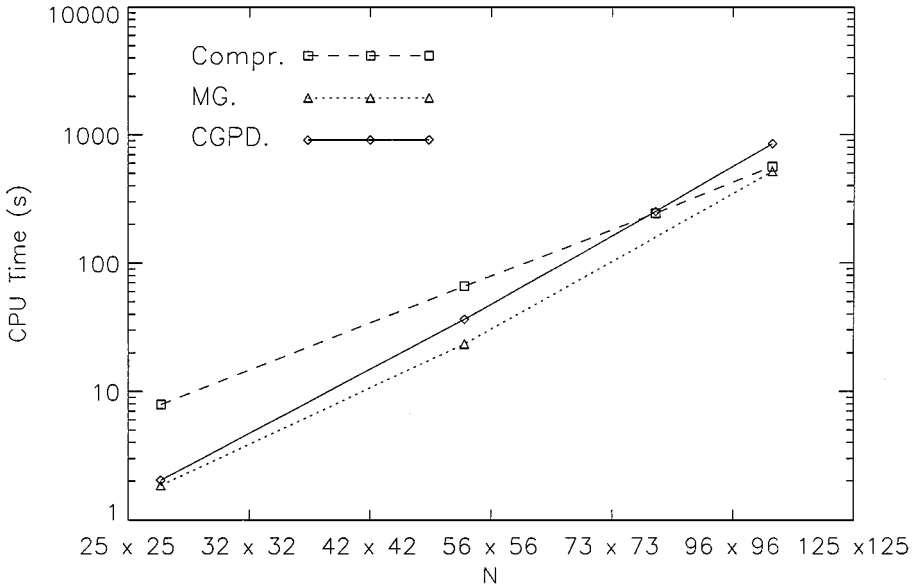

FIG. 15. Vortex spin-down efficiency comparisons. CPU measurements for WCSPH (Compr.), multi-grid PSPH (MG), and the conjugate gradient PSPH Projection with diagonal pre-conditioner (CGPD).

This is due in part to the fact that the diffusion time-step constraint becomes more severe with resolution, but it is also due to the increasing work required per time-step. In both the multi-grid projection and weakly compressible techniques, the work per time-step was $O(N)$ (since the multi-grid method obtained mesh independent convergence rates) whereas for the conjugate gradient method, the number of iterations required for convergence per time-step increased with resolution.

3.4. Convergence Analysis

A convergence analysis was performed for the vortex spin-down problem for PSPH and WCSPH at times $t = 1.0$ through to $t = 5.0$. This analysis was performed in a manner similar to that in which the analyses were done in [5, 30]. For the PSPH technique, at a given time, a solution was computed on particle lattices 27×27, 53×53, and 105×105. In order to remove the effect of time discretization errors, a uniform time-step $\Delta t = 0.001$ was used for all resolutions. An estimate of the L^1 and L^2 errors for the velocity on the 27×27 lattice can be obtained by interpolating the velocities from the 53×53 lattice onto the 27×27 lattice (using the quartic spline kernel given in (6)) and finding the difference between these interpolated velocities and the actual velocities on the 27×27 lattice. Similarly, an estimate of the errors on the 53×53 lattice can be obtained using the velocities on the 105×105 lattice. Table I provides the convergence results for the PSPH technique. At no time is $O(\Delta x^2)$ accuracy recorded with convergence rates of $O(\Delta x^{1.5})$ to $O(\Delta x^{1.0})$ obtained for both L^1 and L^2 norms. The convergence rate decreases as the integration time increases and particles become more disordered.

The same convergence analysis was performed on the WCSPH technique using particle lattices 32×32, 64×64, and 128×128 and a uniform time-step $\Delta t = 5.0 \times 10^{-4}$. Table II provides the results as in the PSPH technique, $O(\Delta x^2)$ accuracy is not observed with

TABLE I
Convergence Results for L^1 and L^2 Velocity Norms Using the PSPH Method with the Quartic Spline Kernel and $h = 1.3\Delta x$

Time	$(27^2 - 53^2)$		$(53^2 - 105^2)$		$Q \to O(\Delta x^Q)$	
	L^1	L^2	L^1	L^2	L^1	L^2
	$\times 10^{-3}$		$\times 10^{-4}$			
1.0	1.043	1.758	3.885	6.866	1.46	1.39
2.0	1.050	1.761	3.837	6.201	1.49	1.55
3.0	0.916	1.547	3.993	6.586	1.23	1.27
4.0	0.866	1.413	4.112	6.566	1.11	1.14
5.0	0.807	1.342	4.183	6.397	0.97	1.10

convergence rates of $O(\Delta x^{1.2})$ to $O(\Delta x^{0.5})$ obtained. The convergence rate also decreases as the integration time increases and particles become more disordered.

Gingold and Monaghan [13] state that $O(h^2)$ truncation error is typically expected in an SPH simulation. However, in this study, $O(h^2)$ accuracy is not obtained for either the L^1 or the L^2 velocity norm for the given spline kernel and smoothing length $h \propto \Delta x$. In fact, Monaghan [21] noted that to obtain $O(\Delta x^2)$ accuracy, a smoothing length $h \propto \Delta x^q$, $q < 1$, is required (assuming that the flow is sufficiently smooth). Similar conclusions were also reached in [29], where a convergence analysis was performed for the vortex method (which uses smoothing kernels to evaluate a convolved velocity field from a discrete set of vortex blobs), and [2], where smoothing kernels were used to evaluate surface tension forces.

To test this assertion further, a convergence analysis for $h \propto \Delta x^{0.5}$ (using $h = 0.23\Delta x^{0.5}$) was performed for the PSPH method on 27×27, 50×50, and 88×88 particle lattices, the results of which are shown in Table III. While the convergence rates do indeed increase, with rates of $O(\Delta x^{1.9})$ to $O(\Delta x^{1.7})$ recorded, $O(\Delta x^2)$ convergence is not observed. This lack of second-order convergence is due to the fact that solid wall boundaries prevent sufficient smoothness in the flow. The boundary conditions used to model these solid walls (see Section 2.5) are also a source of error leading to further reductions in convergence rate. To isolate the effect of the solid wall boundary conditions on convergence rate, a convergence analysis for the spin-down with doubly periodic boundary conditions was performed using PSPH. The use of periodic boundary conditions resulted in higher convergence rates for smoothing lengths $h = 1.3\Delta x$ and $h = 0.23\Delta x^{0.5}$. Rates of $O(\Delta x^{1.4})$ were consistently

TABLE II
Convergence Results for L^1 and L^2 Velocity Norms Using the WCSPH Method with the Quartic Spline Kernel and $h = 1.3\Delta x$

Time	$(32^2 - 64^2)$		$(64^2 - 128^2)$		$Q \to O(\Delta x^Q)$	
	L^1	L^2	L^1	L^2	L^1	L^2
	$\times 10^{-3}$		$\times 10^{-3}$			
1.0	6.991	8.762	2.956	3.824	1.24	1.20
2.0	5.694	7.332	2.541	3.301	1.16	1.15
3.0	4.397	5.902	2.126	2.778	1.05	1.09
4.0	3.100	4.472	1.711	2.255	0.86	0.99
5.0	1.863	3.042	1.296	1.732	0.52	0.81

TABLE III
Convergence Results for L^1 and L^2 Velocity Norms Using the PSPH Method with the Quartic Spline Kernel and $h = 0.23\Delta x^{0.5}$

Time	$(27^2 - 50^2)$		$(50^2 - 88^2)$		$Q \to O(\Delta x^Q)$	
	L^1	L^2	L^1	L^2	L^1	L^2
	$\times 10^{-3}$		$\times 10^{-4}$			
1.0	0.723	1.286	2.670	5.050	1.72	1.61
2.0	0.768	1.285	2.520	4.500	1.92	1.81
3.0	0.803	1.338	2.913	4.771	1.75	1.78
4.0	0.930	1.534	3.350	5.162	1.76	1.89
5.0	0.983	1.600	3.631	5.490	1.72	1.84

observed for $h = 1.3\Delta x$ while for $h = 0.23\Delta x^{0.5}$, convergence rates over $O(\Delta x^2)$ were observed.

4. CONCLUSIONS

The results presented in this study indicate that the PSPH technique has the potential to simulate moderate *Re* incompressible flows more accurately and more efficiently than the present WCSPH technique. Its primary advantage is that it eliminates the requirements of a sound speed and the problems associated with it (such as a restrictive Courant time-step control) and is an alternative tool in analyzing the performance of SPH in the incompressible environment.

Extensions of the technique to complicated domains are relatively straightforward, with the main difficulties being a more generalized boundary treatment for the gradient, projection, and viscous operators and implementation of an efficient elliptic solver. However, further development of the method is required before it becomes a useful tool in simulating incompressible fluid flows, particularly in the areas related to error accumulation in the density field. It is possible that a different choice of projection operator may be one area that could reduce this error accumulation. Additional work is also needed for cases involving free surfaces and inflow and outflow boundary conditions.

ACKNOWLEDGMENTS

The authors acknowledge the assistance and insight of Professor Joe Monaghan of the Department of Mathematics and Statistics, Monash University, Clayton, and Dr. Paul Cleary of CSIRO Mathematical and Information Sciences during the course of the work.

REFERENCES

1. S. Abdallah, Numerical solutions for the pressure Poisson equation with Neumann boundary conditions using a non-staggered grid, 1, *J. Comput. Phys.* **70**, 182 (1987).
2. I. Aleinov and E. G. Puckett, Computing surface tension with high-order kernels, in *Proceedings, International Symposium on Computational Fluid Dynamics, Lake Tahoe, CA, 1995*, edited by K. Oshima.
3. G. K. Batchelor, *An Introduction to Fluid Dynamics* (Cambridge Univ. Press, Cambridge, UK, 1973).
4. J. B. Bell, P. Colella, and H. Glaz, A second-order projection method for the incompressible Navier–Stokes equations, *J. Comput. Phys.* **85**, 257 (1989).

5. J. B. Bell and D. L. Marcus, A second-order projection method for variable density flows, *J. Comput. Phys.* **101**, 334 (1992).
6. W. R. Briley, Numerical method for predicting three-dimensional steady viscous flow in ducts, *J. Comput. Phys.* **14**, 8 (1974).
7. A. J. Chorin, Numerical solution of the Navier–Stokes equations, *J. Math. Comp.* **22**, 745 (1968).
8. P. W. Cleary, *Conduction 2: 2-D Heat Conduction—Accuracy, Resolution and Timesteps*, SPH Technical Note 6, CSIRO Division of Mathematics and Statistics Technical Report DMS-C 95/43. [unpublished]
9. P. W. Cleary, *New Implementation of Viscosity: Tests with Couette Flows*, SPH Technical Note 8, CSIRO Division of Mathematics and Statistics Technical Report DMS-C 96/32. [unpublished]
10. P. W. Cleary, *Improved Boundary Modelling for Ideal Gases Using Explicit Static Boundary Pressures, Fluid Behaviour for Different Equations of State and Instabilities*, Technical Report CMIS, CSIRO Division of Mathematics and Statistics Technical Report CMIS-C 35/97. [unpublished]
11. S. J. Cummins and M. J. Rudman, Solving the Navier Stokes equations using an exact projection method, *Austral. Math. Soc. Gazette* **25**, 200 (1997).
12. R. A. Gingold and J. J. Monaghan, Smoothed particle hydrodynamics: Theory and application to non-spherical stars, *Mon. Not. R. Astron. Soc.* **181**, 181 (1977).
13. R. A. Gingold and J. J. Monaghan, Kernel estimates as a basis for general particle methods in hydrodynamics, *J. Comput. Phys.* **46**, 429 (1982).
14. P. M. Gresho, On the theory of semi-implicit projection methods for viscous incompressible flow and its implementation via a finite element method that also introduces a nearly consistent mass matrix, 1, *Int. J. Numer. Methods Fluids* **4**, 557 (1990).
15. P. M. Gresho and R. L. Sani, On pressure boundary conditions for the incompressible Navier–Stokes equations, *Int. J. Numer. Methods Fluids* **7**, 1111 (1987).
16. Wm. G. Hoover, Isomorphism linking smooth particles and embedded atoms, *Physica A* **260**, 244 (1998).
17. S. Koshizuka, Y. Oka, and H. Tamako, A particle method for calculating splashing of incompressible viscous fluid, in *Proceedings, International Conference on Mathematics and Computations, Reactor Physics and Environmental Analyses, ANS, La Grange Park, IL, 1995*, Vol. 2, p. 1514.
18. S. Koshizuka, A. Nobe, and Y. Oka, Numerical analysis of breaking waves using the moving particle semi-implicit method, *Int. J. Numer. Methods Fluids* **26**, 751 (1998).
19. G. Lapanta and J. U. Brackbill, Control of the number of particles in fluid and MHD particle in cell methods, *Comput. Phys. Commun.* **87**, 139 (1995).
20. L. B. Lucy, A numerical approach to the testing of fission hypothesis, *Astron. J.* **82**, 1013 (1977).
21. J. J. Monaghan, *Smoothed Particle Hydrodynamics 1998*, Applied Mathematics Reports and Preprints, 98/12, Monash University, Melbourne, Australia, 1998. [unpublished]
22. J. J. Monaghan, *Heat Conduction with Discontinuous Conductivity*, Applied Mathematics Reports and Preprints, 95/18, Monash University, Melbourne, Australia, 1995. [unpublished]
23. J. J. Monaghan and A. Kocharyan, SPH simulation of multi-phase flow, *Comput. Phys. Commun.* **87**, 225 (1995).
24. J. J. Monaghan, Simulating free surface flows with SPH, *J. Comput. Phys.* **110**, 399 (1994).
25. J. J. Monaghan, Smoothed particle hydrodynamics, *Annu. Rev. Astron. Astrophys.* **30**, 543 (1992).
26. J. J. Monaghan, The dynamics of interstellar cloud complexes, *Mon. Not. R. Astron. Soc.* **231**, 515 (1988).
27. J. P. Morris, P. J. Fox, and Y. Zhu, Modeling low Reynolds number incompressible flows using SPH, *J. Comput. Phys.* **136**, 214 (1997).
28. J. P. Morris, *A Study of the Stability Properties of SPH*, Applied Mathematics Reports and Preprints, 94/22, Monash University, Melbourne, Australia, 1994. [unpublished]
29. H. O. Nordmark, Rezoning for higher order vortex methods, *J. Comput. Phys.* **97**, 366 (1991).
30. W. J. Rider, *Approximate Projection Methods for Incompressible Flow: Implementation, Variants and Robustness*, LA-UR-2000, Los Alamos National Laboratory, 1995. [unpublished]

31. P. A. Russell and S. Abdallah, Dilation-free solutions for the incompressible flow equations on nonstaggered grid, *AIAA Paper* **35**, 585 (1996).
32. R. L. Sani, P. M. Gresho, R. L. Lee, and D. F. Griffiths, The cause and cure(?) of the spurious pressures generated by certain FEM solutions of the incompressible Navier–Stokes equations, 1, *Int. J. Numer. Methods Fluids* **1**, 17 (1981).
33. J. C. Strikwerda, Finite difference methods for the Stokes and Navier–Stokes equations, *Siam J. Sci. Statist. Comput.* **5**, 56 (1984).
34. J. W. Swegle and S. W. Attaway, *On the Feasibility of Using Smoothed Particle Hydrodynamics for Underwater Explosion Calculations*, Sandia National Laboratories Report, SAND95-0311, 1995.